euspen's 24th International Conference & Exhibition, Dublin, IE, June 2024
www.euspen.eu

Single-shot transmission Differential Interference Contrast Microscopes using LC Savart prism as the shear device

Shyh-Tsong Lin* and Ting-Yu Chien

Department of Electro-optical Engineering, National Taipei University of Technology, 1, Sec.3, Chung-Hsiao East Road, Taipei 10608, Taiwan

**Corresponding author e-mail address: f10402@ntut.edu.tw*

Abstract

Four types of Differential Interference Contrast Microscopes (DICMs) have been verified feasible, the first one uses a pair of Normaski prisms, the second utilizes a Savart prism, the third adopts a cyclic apparatus, and the fourth employs a pair of twisted nematic liquid-crystal cells as the shear device; however, they all require a mechanical movement to switch shear directions; consequently their inspection throughput is decreased in case shear direction switching is necessary during the inspections. An innovative transmission DICM is therefore proposed in this research. It is the same as a single-shot phase-shifting polarizing microscope except it has a liquid-crystal Savart prism inserted in between the objective and sample, and it possesses the advantages of switching shear directions non-mechanically and completing the inspection in a single-shot time. This paper is to introduce the configuration, examination theory, and experimental setup of the DICM; it also exhibits the experimental results from the uses of the setup; the results confirm the function and advantages of the DICM.

Keywords: Differential Interference Contrast Microscope (DICM); liquid-crystal Savart prism; single-shot phase-shifting polarizing microscope

1. Introduction

We have already known that optical microscopy for enhancing image contrast can be implemented using Dark-Field Microscopes (DFMs), Phase-Contrast Microscopes (PCMs), and, DIfferential Interference Contrast Microscopes (DICMs), where DICMs are with the advantage of revealing more sample features (e.g. surface roughness, slope, etc.). Up to date, four types of DICMs have been verified feasible, the first one [1-7] uses a pair of Normaski prisms, the second [8-10] utilizes a Savart prism, the third [11-12] adopts a cyclic apparatus, and the fourth [18] employs a pair of twisted nematic Liquid-Crystal (LC) cells as the shear device; however, they all require a mechanical movement to switch shear directions; consequently their inspection throughput is decreased in case shear direction switching is necessary during the inspections.

An innovative DICM is therefore proposed in this research. It is the same as a single-shot phase-shifting polarizing microscope except that it adopts a novel LC Savart prism, inserted in between the objective and sample, as the shear device, it switches the shear directions by just adjusting the driving voltage of the LC Savart prism, and it is able to achieve living-sample inspections. This paper sequentially introduces the configuration, examination theory, and experimental setup of the proposed DICM, in addition to the experiments and experimental results conducted by the experimental setup. This paper then concludes the research by summarizing the inspection performance of the proposed DICM.

2. The proposed DICM

As that shown in Fig. 1(a), the proposed DICM is composed of a broad-band light source (BLS), polarizer (P) with its transmission axis at 45° measured from the x-axis, color filter (CF), condenser lens (C) with a small numerical aperture, reflecting mirror (M), objective (O), tube lens (TL), quarter-wave plate (QWP) with its fast axis at 45° measured from the x-axis, and CMOS sensor equipped with an analyzer composed of repeated arrays of 2×2 pixelated polarizers. In addition, an LC Savart prism (LCSP) is placed between the objective and sample (S). A magnified 3D drawing of the LC Savart prism is exhibited in Fig. 1(b), it demonstrates that the prism is made up of two anti-parallel alignment LC cells (LC_x and LC_y), which are with their respective driving powers and their principal sections (plane containing prism surface normal and optic axis) parallel to x-z and y-z planes, respectively.

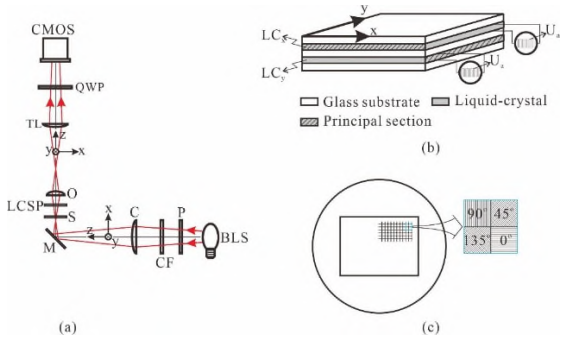

Figure 1 (a) Schematic of the proposed DICM; (b) 3D drawing demonstrating the LC Savart prism; (c) CMOS sensor viewed along the z-axis, where the polarizers of one array are marked to indicate their respective transmission axis orientations.

The optics pertaining to uniaxial birefriengent crystals has been analyzed in detail in Refs. [13, 14], by which the effects of each LC cell of the LC Savart prism on an incident ray are summarized and interpreted as follows. As that shown in Fig. 2(a), when LC_x is driven by an AC voltage with an amplitude of U_a (e.g. U_a = 3.5 V), its optic axis (i.e. the long axis of the LC molecules) moves to a direction having an angle β with respect

to the cell surface normal [15, 16], it can therefore shear an incident ray with a small incident angle into two rays (o- and e-rays), whose propagation direction is parallel to that of the incident ray and whose shear direction is along the x-axis, having a shear distance and Optical-Path-Difference (OPD) of

$$\Delta x = t\frac{(n_o^2 - n_e^2)\sin\beta\cos\beta}{A} \quad (1)$$

and

$$\Lambda_0 = t\left(\frac{n_o n_e}{A^{1/2}} - n_o\right), \quad (2)$$

respectively; where **t** represents the thickness of the LC layer, $\mathbf{n_o}$ and $\mathbf{n_e}$ are the ordinary and extraordinary refractive indices, respectively, of the LC material, and

$$A = n_o^2\sin^2\beta + n_e^2\cos^2\beta. \quad (3)$$

Nevertheless, as the phenomenon demonstrated using Fig. 2(b), when the amplitude of the driving voltage increases to an adequately high value (e.g. $U_a \geqq 10$ V), the optic axis displaces to the direction parallel to the cell surface normal (i.e. $\beta \approx 0^o$), accordingly the shear distance disappears and the corresponding OPD becomes zero.

Figs. 2(a) and 2(b) are respectively called the turned on and turned off states of the LC cell and represented as LC_x=1 and LC_x=0 hereafter.

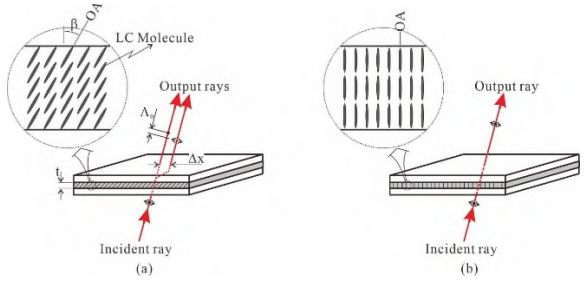

Figure 2 (a) Turned on and (b) turned off states of LC_x; where.and ↔ represent o- and e-rays, respectively.

Like LC_x, the turn on and turn off states of LC_y are represented as LC_y=1 and LC_y=0, respectively.The effects of LC_y on an incident ray are the same as those of LC_x except that its shear direction is along the y-axis. By using the above-described effects, the inspections using the proposed microscope are demonstrated as follows. Referring to Fig. 1(a) again, where the polarizer and color filter convert the light beam from the light source into a linearly polarized and adequately band-narrowed beam, the condenser collects the beam emerging from the color filter to illuminate the sample and then pass through the LC Savart prism, and the objective collects the light beam emanating from the LC Savart prism to propagate through the tube lens and quarter-wave plate to generate an image on the CMOS sensor.

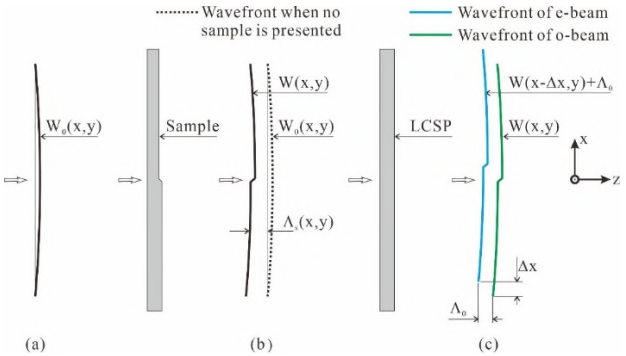

Figure 3 Evolution of wavefronts propagating through the sample and then LC Savart prism.

As LC_x = 1 and LC_y = 0, the image on the CMOS sensor can be illustrated via Fig.3; where (a) shows the wavefront, i.e. $W_0(x, y)$, of the beam incident on the sample; (b) presents the wavefront, i.e. W (x, y) which is the superposition of $W_0(x, y)$ and $\Lambda_s(x,y)$, of the beam emerging from the sample; and (c) depicts the wavefronts, i.e. W (x-Δx, y)+Λ_0 and W (x, y), of the sheared beams emanating from the LC Savart prism, the lateral shear, Δx, and longitudinal lag, Λ_0, are due to the above-mentioned effects contributed by LC_x. Fig. 3 gives that the sheared beams are with an OPD of

$$\Lambda = W(x,y) - [W(x-\Delta x, y) + \Lambda_0] \quad (3a)$$

or, since W (x, y) = $W_0(x, y) + \Lambda_s(x,y)$,

$$\Lambda = \Delta W_0(x,y) + \Delta\Lambda_s(x,y) - \Lambda_0; \quad (3b)$$

where $\Lambda_s(x,y)$ stands for the Optical Path Length (OPL) of the sample, $\Delta W_0(x,y) = W_0(x,y) - W_0(x-\Delta x, y)$, and $\Delta\Lambda_s(x,y) = \Lambda_s(x,y) - \Lambda_s(x-\Delta x, y)$. Correspondingly, the image on the CMOS sensor has an interference intensity of

$$I = I_0[1 + \cos(\frac{2\pi}{\lambda}\Lambda + 2\alpha)], \quad (4)$$

where λ represents the central wavelength of the light beams and α denotes the transmission axis angle of the analyzer where the interference beams pass through [17, 18]. Substituting Eq. (3b) into Eq. (4) leads to

$$I = I_0[1 + \cos(\Delta\phi + \tau + 2\alpha)], \quad (5)$$

where

$$\Delta\phi = \frac{2\pi}{\lambda}\Delta\Lambda_s(x,y) \quad (6)$$

and

$$\tau = \frac{2\pi}{\lambda}[\Delta W_0(x,y) - \Lambda_0]. \quad (7)$$

Eq. (5) agrees that the configuration of Fig. 1(a) is a DICM, since its phase is a function of OPL variation of the sample. The only difference of this equation from that of conventional DICMs is the existence of phase **τ**, which is independent of the sample and can be eliminated using the subtraction method.

When LC_x = 0 and LC_y = 1, the image on the CMOS sensor can also be interpreted via Fig.3, and a derivation gives an image intensity the same as Eq. (5) except that the lateral shear is along the y-axis.

The images corresponding to Eqs. (5) and (6) are referred to as the Differential Interference Contrast (DIC) image and phase-DIC image, respectively. Be aware that, as that demonstrated in Fig. 1 (c), a single-shot image grabbed by the CMOS sensor can be separated into four DIC-images with α=0°, 45°, 90°, and 135°, respectively; by which, the phase-DIC image can be obtained using the four-step phase-shifting technique [19, 20] incorporated with the subtraction method, i.e.,

$$\Delta\phi = \tan 2\left(\frac{\mathbf{I}_4 - \mathbf{I}_2}{\mathbf{I}_1 - \mathbf{I}_3}\right) - \tau \; ; \qquad (8)$$

where $\mathbf{I_1}$, $\mathbf{I_2}$, $\mathbf{I_3}$, and $\mathbf{I_4}$ stand for the DIC images with α=0°, 45°, 90°, and 135°, respectively, and τ is pre-determined by the same four-step phase-shifting technique when no sample is presented.

.

3. Experimental setup

To implement the proposed DICM, a setup comprising the proposed DICM and a control and image processing system was installed, where the control and image processing system comprised a dual-channel function generator, DG 1022 from RIGOL Technologies, Inc., China, and a personal computer.

In the DICM, the light source was a halogen lamp, the condenser had a numerical aperture of 0.05, the color filter output a red-light beam with a central wavelength of 648nm, the objective was CFI Plan Flour ELWD 20xC (NA = 0.45, cover glass compensation: 0-2.0 mm) from Nikon Corp., Japan, the tube lens was MT-1 from Nikon Corp., Japan, the quarter-wave plate was of a broadband type obtained from the Photoelastic Division of Measurements Group, Inc., USA, the CMOS sensor was BFS-U3-51S5P-C from FLIR Integrated Imaging Solutions Inc., Canada, and the LC Savart prism was fabricated at the liquid crystal lab of the authors' department.

In the control and image processing system, the two channels of the function generator were utilized as the driving powers of the LC Savart prism, and each of them exported a one kHz rectangular-wave voltage with U_a = 3.5 V/ 10.0 V to turn on/ off its corresponding LC cell; the computer executed three programs: image grabbing, evaluation, and display. The image grabbing involved acquiring the DIC images on the CMOS sensor and storing them in the memory of the computer; the evaluation extracted the phase-DIC images by the uses of Eq. (8) and the stored images; and the display exhibited the obtained DIC and phase-DIC images on the computer monitor.

4. Experimental results

To verify the proposed DICM, two experiments were carried out. The first conducted the setup to inspect a 2-D rectangular grating made of quartz. The DIC images grabbed as LC_x = 1 and LC_y = 0 are illustrated in Fig.4 (a). The phase-DIC image calculated using the DIC images of Fig. 4(a) and Eq. (8) is presented in Fig. 4(b). The DIC images captured as LC_x =0 and LC_y =1 are exhibited in Fig.5 (a). And the phase-DIC image determined using the DIC images of Fig. 5(a) and Eq. (8) is revealed in Fig. 5(b). Figs. 4 (b) and 5(b) confirm the function of the proposed DICM, since they are consistent with the predicted x- and y-shearing phase-DIC images, respectively, of the 2-D rectangular grating. According to Eq. (6), the x-shearing phase-DIC image of the 2-D rectangular grating is predicted to be with positive and negative phases at vertical low-to-height and high-to-low edges, respectively; whereas the y-shearing image is predicted to be with positive and negative phases at horizontal low-to-height and high-to-low edges, respectively.

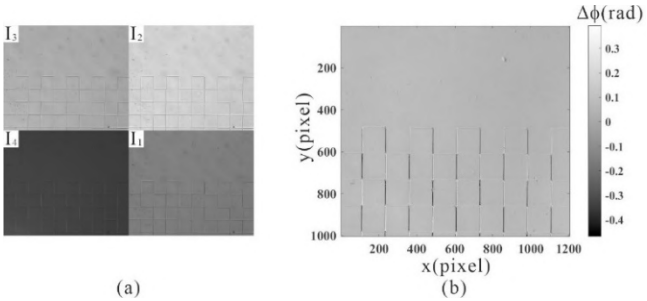

Figure 4 Inspection results when LC_x = 1 and LC_y = 0. (a) Grabbed DIC images; (b) calculated phase-DIC image; where each image is with a size of 1224×1024 pixels, and each pixel represents a length of 0.348 μm.

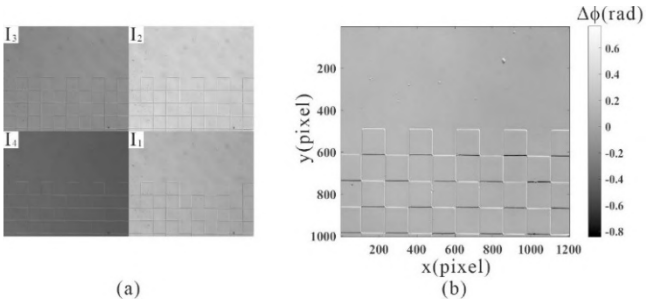

Figure 5 Inspection results when LC_x =0 and LC_y =1. (a) Grabbed DIC images; (b) calculated phase-DIC image.

The second experiment was to examine an unstained onion epidermal tissue, sandwiched in between a slide and a cover slip. The obtained x- and y-shearing phase-DIC images are shown in Figs. 6 (a) and (b) respectively, illustrating the proposed DICM is capable of retrieving more detailed images/features of the sample than the equivalent bright-field image shown in Fig. 6(c). On examining these images, Figs. 6 (a) and (b) clearly exhibit the tissue's nuclei, however Fig. 6 (c), the bright-field image of the same sample, fails to distinguish the nuclei.

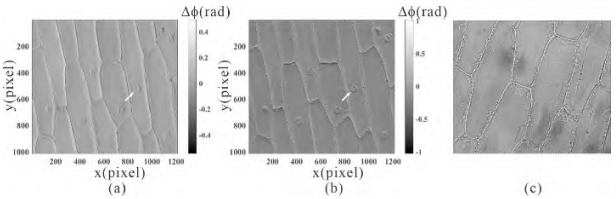

Figure 6 (a) X-shearing phase-DIC image, (b) y-shearing phase-DIC image, and (c) bright-field image of an onion epidermal tissue. The white arrows direct to a nucleus of the tissue; the field of (c) is not the same as that of (a) and (b)

5. Discussions

Furthermore, the above experiments verify that the proposed DICM can not only switch the shear directions by adjusting the driving voltage of the LC Savart prism, but also obtain the phase-DIC image by using a single-shot image; the latter endows the DICM with the ability of living-sample inspections. To verify this ability, an experiment conducting the setup to examine a paramecium solution sandwiched in between a slide and a cover slip was accomplished, where the computer recorded the images on the CMOS sensor for 2 seconds at 25fps and then converted the recorded images into their respective phase-DIC images. 6 images of the obtained y-shearing phase-DIC images are exhibited in Fig. 7, confirming the living-sample inspection ability of the proposed DICM.

Referring to Fig. 1 again, the DICM can be enhanced by inserting a beam-splitter between the objective and tube lens, and placing a module composed of a broad-band light source, polarizer, color filter, and condenser lens on the right-hand side of the beam-splitter. With this enhancement, the DICM will be capable of both reflection and transmission inspections. The authors are now installing a setup implementing this enhancement.

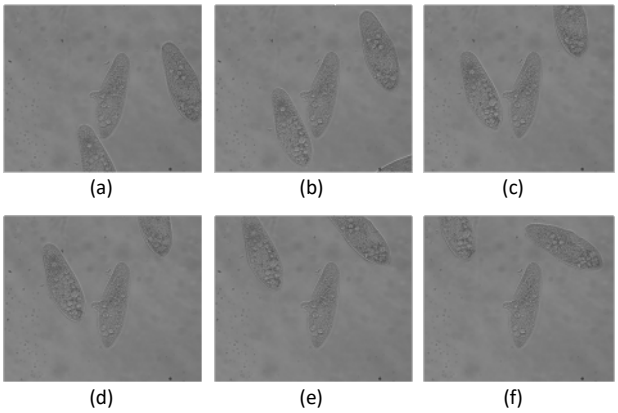

Figure 7 (a)-(f) y-shearing phase-DIC images of a paramecium solution.

6. Conclusions

An innovative transmission DICM using LC Savart prism as the shear device has been developed for retrieving images with OPL variation information. In addition to the intended advantage of switching the shear directions without mechanical movements, it also provides a superior ability over conventional DICMs of living-sample inspections. This paper has introduced the detail of the DICM, exhibited the setup for implementing the DICM, and performed the experimental tests and assessed the results achieved; which not only confirmed the intended functionality but also its additional advantages achieved.

Acknowledgments

The support of Ministry of Science and Technology, Taiwan, ROC under grant MOST 108-2221-E-027-101 is gratefully acknowledged.

References

[1] D. L. Lessor, J. S. Hartman, and R. L. Gordon, "Quantitative surface topography determination by Nomarski reflection microscopy. I. Theory," J. Opt. Soc. Am. 69, pp. 357-366 (1979).

[2] J. S. Hartman, R. L. Gordon, and D. L. Lessor, "Quantitative surface topography determination by Nomarski reflection microscopy. 2: Microscope modification, calibration, and planar sample experiments," Appl. Opt. 19, pp.2998-3009 (1980).

[3] J. S. Hartman, R. L. Gordon, and D. L. Lessor, "Nomarski differential interference contrast microscopy for surface slope measurements: an examination of techniques," Appl. Opt. 20, pp.2665-2669 (1981).

[4] S. N. Jabr, "Surface-roughness measurement by digital processing of Nomarski phase-contrast images," Opt. Lett. 10, pp. 526-528 (1985).

[5] T. R. Corle and G. S. Kino, "Differential interference contrast imaging on a real time confocal scanning optical microscope," Appl. Opt. 29, pp.3769-3774 (1990).

[6] S. V. King, A. Libertun, R. Piestun, C. J. Cogswell, and C. Preza, "Quantitative phase microscopy through differential interference imaging," J. Biomed. Opt. 13, pp. 024020 (2008).

[7] A. Serrano-Trujillo, A. Nava-Vega, and V. Ruiz-Cortez, "Development of a polarimetric experimental setup for surface profiling based on a microscopy application," Proc. SPIE 9598, pp. 95981H (2015).

[8] M. Françon, "Polarization apparatus for interference microscopy and macroscopy of isotropic transparent objects," J. Opt. Soc. Am. 47, pp. 528-535 (1957).

[9] H. X. Trịnh, S. T. Lin, L. C. Chen, S. L. Yeh, and C. S. Chen, "Differential interference contrast microscopy using Savart plates," J. Opt. (United Kingdom) 19, pp. 045601 (2017).

[10] S. T. Lin, H. X. Trinh, Z. W. Chen, and T. H. Lee, "Phase-shifting differential interference contrast microscope with Savart shear prism and rotatable analyser," J. Microsc.272, pp.79-84 (2018).

[11] S. Chatterjee and Y. P. Kumar, "White light differential interference contrast microscope with a Sagnac interferometer," Appl. Opt. 53, pp.296-300 (2014).

[12] S. Chatterjee and Y. P. Kumar, "Un-polarized light transmission DIC microscope," J. Opt. (India) 45, pp. 297-301(2016).

[13] M. Francon and S. Mallick, Polarization interferometers, Wiley-Interscience, New York, 1971.

[14] L. Wu, C. Zhang, Y. Yuan, and B. Zhao, "Exact calculation of lateral displacement and optical path difference of Savart polariscopes," Acta Optica Sinica 25, pp. 885-890 (2005).

[15] P. D. Berezin, I. N. Kompanets, V. V. Nikitin, and S. A. Pikin, "Orienting effect of an electric field on nematic liquid crystals," Sov. Phys.-JETP 37, pp. 305-308 (1973).

[16] E. Hecht, Optics, 5th Ed., Pearson, New York, 2017.

[17] S. Suja Helen, M. P. Kothiyal, and R. S. Sirohi, "Achromatic phase shifting by a rotating polarizer," Opt. Commun. 154, pp. 249–254(1998).

[18] S. Mukhopadhyay, S. Sarkar, K. Bhattacharya, and L. Hazra, "Polarization phase shifting interferometric technique for phase calibration of a reflective phase spatial light modulator," Opt. Eng. 52, pp. 035602 (2013).

[19] J. Millerd, N. Brock, J. Hayes, B. Kimbrough, M. North-Morris, and J. C. Wyant, "Vibration insensitive interferometry," Proc. SPIE 10567, pp. 105671P (2006).

[20] J. W. Jeon and K. N. Joo, "Single-shot imaging of two-wavelength spatial phase-shifting interferometry," Sensors 19, pp. 5094 (2019).